Supplementary Material

Dopant-Driven Electronic and Lattice Softening Enables Transport-Coupled CO_2 Reduction in β-Ag_2Se

Sathish Panneer Selvam [a*], Kyusik Yun [b], Sungbo Cho [a,c,d*]

[a]*Department of Electronic Engineering, Gachon University, Seongnam-si, Gyeonggi-do 13120, Korea*

[b]*Department of Bionanotechnology, Gachon University, Seongnam-si, Gyeonggi-do 13120, Korea*

[c]*Department of Semiconductor Engineering, Gachon University, Seongnam-si, Gyeonggi-do 13120, Korea*

[d]*Gachon Advanced Institute for Health Science & Technology, Gachon University, Incheon 21999, Korea*

***Corresponding author:**

* Sathish Panneer Selvam: satp103@gachon.ac.kr

* Sungbo Cho: sbcho@gachon.ac.kr

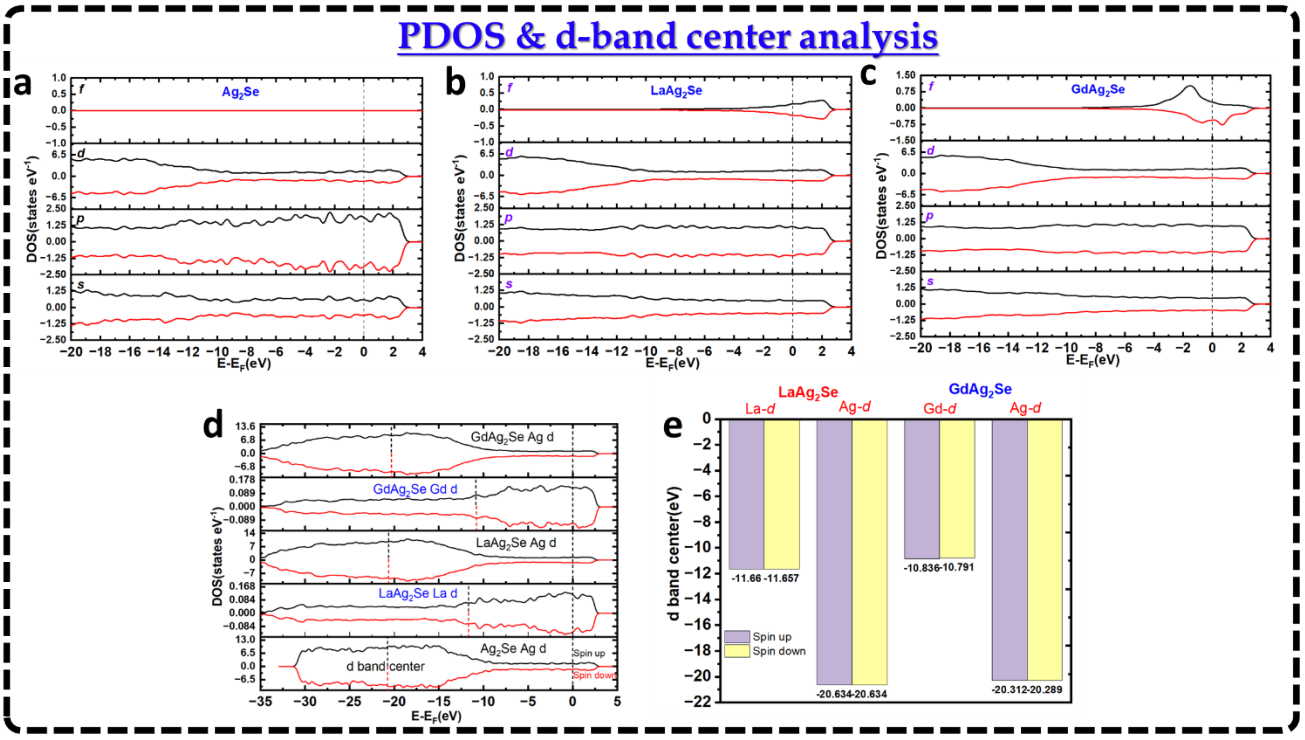

Fig. S1 Analysis of spin-resolved projected density of states (PDOS) and d-band center for pristine Ag_2Se and lanthanide-doped systems. (a–c) Orbital-resolved projected density of states (PDOS) illustrating s, p, d, and f contributions in relation to the Fermi level, emphasising electronic redistribution generated by dopants and increased hybridisation near the Fermi level. (d) Comparative distributions of spin-polarized Ag-d and dopant d-states demonstrating alterations in electronic occupancy. Calculated d-band centers for Ag, La, and Gd components, demonstrating dopant-dependent modulation of d-state energetics. The findings illustrate how the introduction of lanthanides modifies the electrical structure and d-band alignment in Ag_2Se.

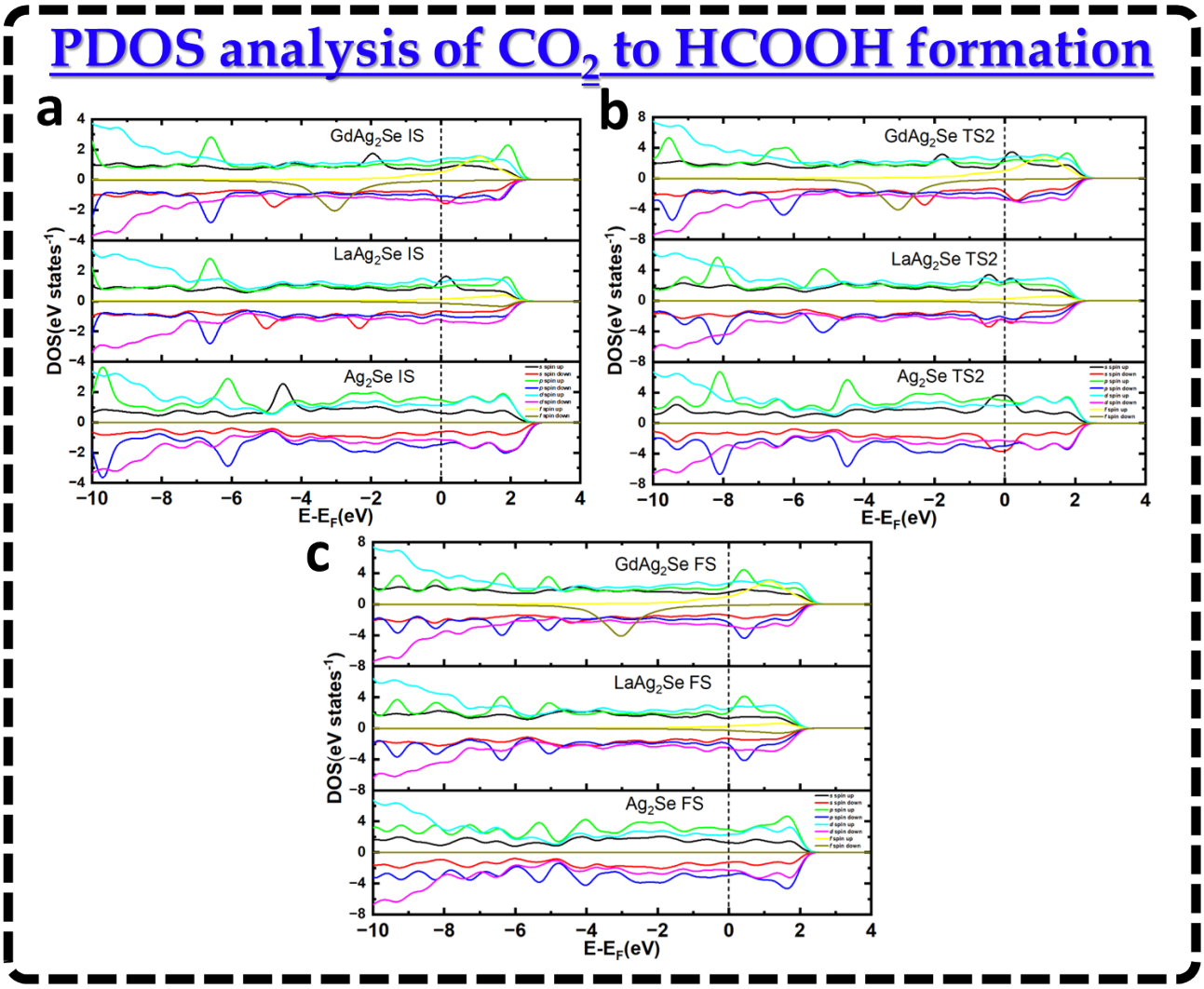

Fig. S2 Spin-resolved projected density of states (PDOS) during the conversion of CO_2 to HCOOH on pristine Ag_2Se and lanthanide-doped surfaces. (a) Initial state (IS), (b) transition state (TS_2), and (c) final state (FS) electronic distributions relative to the Fermi level. The hybridisation of orbitals and charge redistribution influenced by dopants around the Fermi energy demonstrate increased electronic involvement and stabilisation of transition states in the doped systems relative to virgin Ag_2Se.

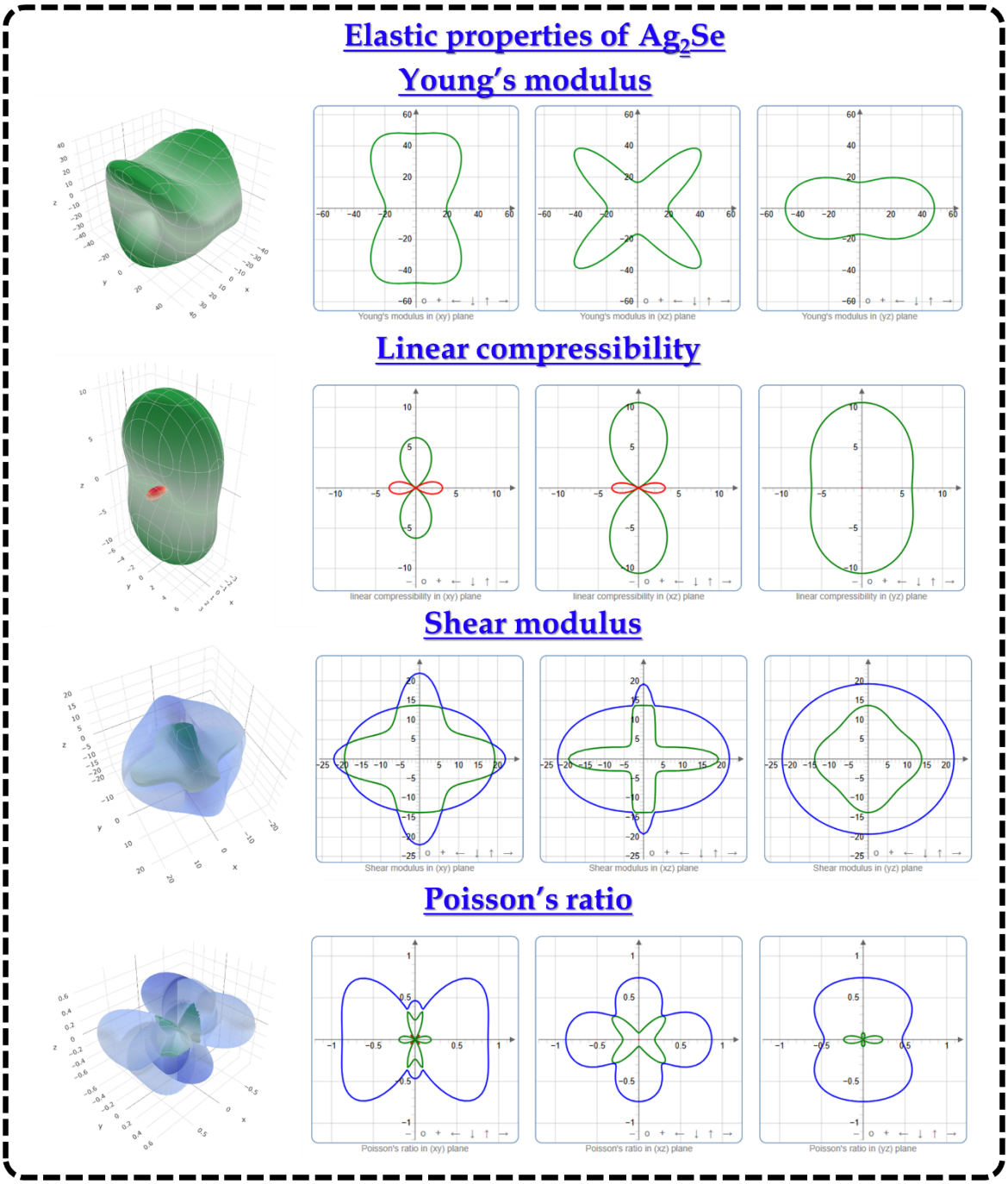

Fig. S3 Directional elastic properties of Ag_2Se derived from the elastic tensor. Three-dimensional surfaces and corresponding planar projections illustrate the anisotropic Young's modulus, linear compressibility, shear modulus, and Poisson's ratio in the principal crystallographic planes. The distributions reveal direction-dependent mechanical response,

highlighting lattice stiffness, compressibility, shear resistance, and strain coupling that govern elastic anisotropy in Ag_2Se.

Table S1 Effective isotropic elastic properties (Hill averages)

Material	Bulk modulus KH (GPa)	Young's modulus EH (GPa)	Shear modulus GH (GPa)	Poisson ratio vH
Ag_2Se	77.284	39.032	13.784	0.4158
$LaAg_2Se$	22.654	23.963	9.051	0.3237
$GdAg_2Se$	52.019	47.887	17.781	0.3466

Table S2 Mechanical stability (stiffness eigenvalues)

Material	λ_1	λ_2	λ_3	λ_4	λ_5	λ_6	Stability
Ag_2Se	9.97	13.73	19.28	22.04	36.51	243.33	Stable
$LaAg_2Se$	5.00	6.94	11.37	21.12	27.86	70.94	Stable (soft lattice)
$GdAg_2Se$	14.00	16.00	18.00	37.50	46.25	158.26	Stable (reinforced)

Table S3 Elastic anisotropy indicators

Material	Young's anisotropy	Compressibility anisotropy	Shear anisotropy	Poisson anisotropy
Ag_2Se	3.277	∞	4.408	∞
$LaAg_2Se$	2.476	2.058	2.686	4.162
$GdAg_2Se$	1.541	1.694	1.573	2.302

Table S4 Elastic range (directional extrema)

Material	Emin–Emax (GPa)	Gmin–Gmax (GPa)	νmin–νmax
Ag_2Se	16.67 – 54.62	5.00 – 22.04	−0.072 – 1.028
$LaAg_2Se$	15.73 – 38.96	5.00 – 13.43	0.140 – 0.585
$GdAg_2Se$	41.46 – 63.88	14.00 – 22.03	0.211 – 0.486